



# Covalent triazine polymer derived porous carbon with high porosity and nitrogen content for bifunctional oxygen catalysis in zinc–air battery

You Tao<sup>a,b</sup>, Dong-Hui Yang<sup>a,\*</sup>, Hui-Yuan Kong<sup>a,b</sup>, Tian-Xiong Wang<sup>a,b</sup>, Zihao Li<sup>a</sup>, Xuesong Ding<sup>a</sup>, Bao-Hang Han<sup>a,b,\*\*</sup>

<sup>a</sup> CAS Key Laboratory of Nanosystem and Hierarchical Fabrication, CAS Center for Excellence in Nanoscience, National Center for Nanoscience and Technology, Beijing 100190, China

<sup>b</sup> University of Chinese Academy of Sciences, Beijing 100049, China

## ARTICLE INFO

### Keywords:

N-doped porous carbon  
High nitrogen content  
Large specific surface area  
Bifunctional oxygen electrocatalysts  
Zinc–air battery

## ABSTRACT

Nitrogen-doped porous carbon possesses widespread applications in energy-related fields due to its unique properties. However, preparation of porous carbon (specific surface area  $> 3000 \text{ m}^2 \text{ g}^{-1}$ ) with high nitrogen content ( $> 10 \text{ wt\%}$ ) remains great challenges because of high synthesis temperature. Herein, a covalent triazine polymer was innovatively designed by cyclotrimerization of tetracyanoethylene, and used to produce the high nitrogen-doped porous carbon. The as-prepared porous carbon (HNPC-900) possesses a high nitrogen content (14.2 wt%) and large specific surface area ( $3210 \text{ m}^2 \text{ g}^{-1}$ ). When HNPC-900 was applied as the air-cathode for zinc–air batteries, it shows a high specific capacity ( $797 \text{ mAh g}_{\text{zn}}^{-1}$ ) and stable rechargeability (more than 380 h over 960 cycles at  $5 \text{ mA cm}^{-2}$ ), outperforming the cathode composed of  $\text{RuO}_2$  and 20 wt% Pt/C. This ingenious design provides a feasible strategy to prepare high nitrogen-doped porous carbon, giving extensive application prospects of porous carbon for catalysis and energy storage fields.

## 1. Introduction

Porous carbon materials with features of large specific surface areas, high electrical conductivity, and good stability, are widely applied in the fields of gas separation, water purification, electromagnetic shielding, retardant, and energy storage and conversion [1–5]. Nowadays, heteroatom-doping (N, P, S, F, Cl, etc.) endows porous carbon materials with fascinating electronic and chemical properties by changing the physicochemical properties of carbon materials [6–10]. As an adjacent element of C in the periodic table, N atom possesses the similar atomic size to C atom and can form stable covalent bond with C atom, and thus becomes the most studied heteroatom over the past decades. The similar bond length of C–N bond ( $1.47 \text{ \AA}$ ) to C–C bond ( $1.54 \text{ \AA}$ ) can minimize the structural distortion and maintain the geometry of the carbon network, which in turn retains the stability of carbon materials [11]. The configuration of doped N atoms can be mainly divided into pyridinic N, pyrrolic N, and quaternary N, which affect the charge density of C due to the strong electronegativity of N element. As a result, the doped N atoms

of carbon materials will transfer electrons around C atoms to N atoms, thereby modulating the electronic structures of carbon materials at N-doped sites, and causing the accumulation of local charges and the change of local electronic density of states, which may effectively promote electron transfer reactions and accelerate the adsorption and/or activation of reactant molecules [12]. Meanwhile, the configuration of doped N atoms is meaningful for porous carbon materials. For instance, quaternary N is suggested improving the limiting current density, while pyridinic N is proposed to play an important role on the onset potential in the oxygen reduction reaction (ORR) [13–18]. Furthermore, the overall positive charge of C atoms adjacent to N atom can enhance the binding energy of  $\text{O}_2$ , which contributes to electrocatalytic performance by changing the  $\text{O}_2$  adsorption mode [19,20]. Aside from the modulation of electronic property, N-doping can regulate acidity–basicity and wettability of carbon materials, improving the interaction between the surface of carbon materials and reactant molecules or reactive species. Inspired by these special properties, N-doped carbon materials have received extensive attention and become a hot research direction in

\* Corresponding author

\*\* Corresponding author at: CAS Key Laboratory of Nanosystem and Hierarchical Fabrication, CAS Center for Excellence in Nanoscience, National Center for Nanoscience and Technology, Beijing 100190, China.

E-mail addresses: [yangdh@nanoctr.cn](mailto:yangdh@nanoctr.cn) (D.-H. Yang), [hanbh@nanoctr.cn](mailto:hanbh@nanoctr.cn) (B.-H. Han).

<https://doi.org/10.1016/j.apcatb.2023.123088>

Received 15 November 2022; Received in revised form 7 June 2023; Accepted 9 July 2023

Available online 11 July 2023

0926-3373/© 2023 Elsevier B.V. All rights reserved.

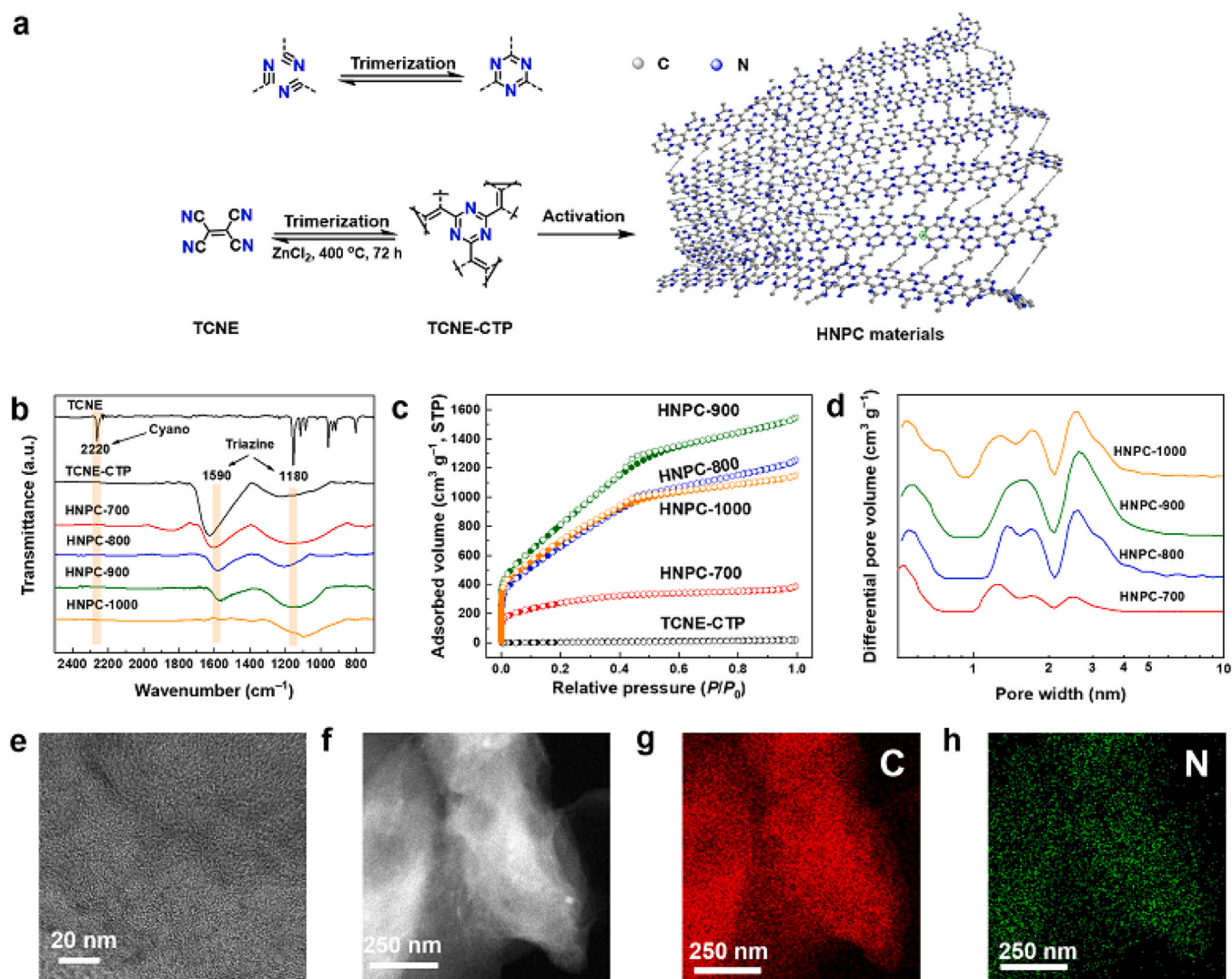


**Fig. 1.** (a) Schematic preparation of HNPC materials. (b) FT-IR spectra of TCNE, TCNE-CTP, and HNPC materials. (c) Nitrogen adsorption-desorption isotherms and (d) pore-size distribution profiles of HNPC materials. (e) HRTEM image of HNPC-900. Scanning transmission electron microscopy image of HNPC-900 (f) and elemental mapping images of C (g) and N (h) of HNPC-900.

terms of electrocatalysis.

Nowadays, the pyrolysis of C- and N-containing precursors under inert atmosphere is a typical strategy to prepare N-doped porous carbon materials. Common precursors mainly include conductive polymers, biomass-based materials, ionic liquids, etc. The templates (e.g., SiO<sub>2</sub>, NaCl, F127) or activating agents (e.g., KOH) are employed in the pyrolysis processes to create hierarchical pores in carbon materials [21–23]. To greatly enhance the porosity of carbon materials, the judicious choice of precursors is of great significance. Among the well-employed precursors, porous organic polymers (POPs) stand out due to the availability of tunable chemical compositions and pore sizes [24]. At present, POPs, including covalent organic frameworks, porous aromatic frameworks, conjugated microporous polymers, hypercrosslinked polymers, and covalent triazine frameworks (CTFs), have been applied as porous precursors to prepare N-doped porous carbon materials [25–33]. For example, a carbon material with 1.42 wt% N derived from a pyrrole-based hypercrosslinked polymer possesses a Brunauer–Emmett–Teller specific surface area ( $S_{\text{BET}}$ ) of 4332 m<sup>2</sup> g<sup>-1</sup> via KOH activation [34]. Among POPs, CTFs pioneered by Antonietti and Thomas [35] are noted as N-containing precursors, which have shown great potential in preparation of N-doped porous carbon materials. CTFs are generally synthesized by cyclotrimerization of cyano-functionalized

building blocks. The formed triazine rings in CTFs provide abundant N sources [36], and the N content of CTFs can be further enhanced by choosing the N-containing and cyano-functionalized building blocks. More importantly, the different N configuration can be achieved in CTF-derived N-doped porous carbon materials, endowing carbon materials with a wide adaptability for different applications [37]. For example, a tetracyanoquinodimethane-based CTF-derived porous carbon with 8.1 wt% N content and a  $S_{\text{BET}}$  of 3663 m<sup>2</sup> g<sup>-1</sup> shows the potential application in supercapacitors [38]. Nevertheless, most CTF-derived carbon materials with high porosity ( $S_{\text{BET}} > 3000$  m<sup>2</sup> g<sup>-1</sup>) possess N contents of much less than 10 wt% up to now [39–48]. The limited N content is not sufficient to offer the chance to exploit the optimal performance of porous carbon materials, and the desired precursors still need further exploration and study to obtain high N-doped porous carbon materials.

Herein, tetracyanoethylene (TCNE), an ethylene unit bearing four  $\pi$ -conjugated nitriles, is carefully selected as the monomer, and a new covalent triazine polymer (named as TCNE-CTP) is successfully prepared via cyclotrimerization. Different from our previous work on synergistic contribution of N and F species in porous carbons for zinc–air batteries (ZABs) [33], this work focuses on the development of new materials with dual-superiority in nitrogen content and porosity.

Notably, the TCNE-CTP-derived high N-doped porous carbon (HNPC) material (HNPC-900) possesses a large  $S_{\text{BET}}$  and a high N content, which are higher than those of all other known POP-derived N-doped porous carbon materials. High N content endows HNPC-900 with excellent electrocatalytic performances for ORR and oxygen evolution reaction (OER). As a bifunctional air-cathode for ZABs, HNPC-900 exhibits a high specific capacity and stable rechargeability.

## 2. Experimental section

### 2.1. Synthesis of TCNE-CTP

TCNE-CTP was synthesized via the typical ionothermal method with extended reaction time for 72 h. Typically, TCNE (1 mmol, 0.13 g) and  $\text{ZnCl}_2$  (10 mmol, 1.36 g) were well-mixed and transferred into a quartz ampoule ( $\Phi$  2 cm  $\times$  12 cm) under  $\text{N}_2$  atmosphere. Subsequently, the ampoule was evacuated, sealed, and heated to 400 °C for 72 h. After cooling down to room temperature, the ampoule was opened and the black monolithic material was obtained. In order to remove  $\text{ZnCl}_2$  and the residual monomers, the resulted black monolithic material was stirred in water, 1 M HCl, and tetrahydrofuran (THF) for 12 h, respectively. The resulting black powder was filtered, extensively washed with 1 M HCl solution and water, and then dried in vacuum at 80 °C for 24 h. TCNE-CTP was obtained with a quantitative yield.

### 2.2. Syntheses of HNPC materials

A series of HNPC materials were synthesized through changing the activation temperature by using KOH as an activating agent under  $\text{N}_2$  atmosphere and keeping at the corresponding temperature for 2 h. After being washed with 1 M HCl solution and water, the obtained HNPC materials were labeled according to the activation temperature (e.g., HNPC-700, HNPC-800, HNPC-900, and HNPC-1000).

### 2.3. Electrochemical measurements

Linear-scan voltammetry (LSV), cyclic voltammetry (CV), electrochemical impedance spectroscopy (EIS), and chronoamperometry ( $i$ -t) measurements were performed by a three-electrode system using AFMSRCE RDE control system (Pine Inc., U.S.A.) on a CHI 760E work station (Shanghai Chenhua, China). For the rotating ring-disk electrode (RRDE) tests, Ag/AgCl, Pt wire, and glassy carbon were used as the reference electrode, the counter electrode, and the working electrode, respectively. The commercial 20 wt% Pt/C and ruthenium(IV) oxide ( $\text{RuO}_2$ ) were used as electrocatalysts for comparison. For the preparation of electrocatalyst ink, the catalyst (2.0 mg) was dispersed in a mixture of Nafion solution (5 wt%, 5  $\mu\text{L}$ ) and ethanol (495  $\mu\text{L}$ ) by ultrasonic dispersion. The well-dispersed ink was dropped on the fresh surface of the working electrode. After evaporating the solvent, a thin electrocatalyst film was then coated on the surface of the glassy carbon electrode. The mass loading of catalyst was about 0.2 mg  $\text{cm}^{-2}$ .

### 2.4. Homemade ZABs

The homemade ZABs were assembled to further evaluate the potential application of HNPC materials. The carbon paper coated by a catalyst with a mass loading of 1.0 mg  $\text{cm}^{-2}$  was used as the air cathode, while the polished Zn plate with a thickness of 0.5 mm was used as the anode. The quality changes of Zn plate before and after galvanostatic discharge tests were used for calculation of specific capacity. The electrolyte solution was the mixture of aqueous KOH solution (6.0 M) and aqueous  $\text{Zn}(\text{Ac})_2$  solution (0.2 M). The gas diffusion layer was assembled by a nickel foam, which was used as the current collector and a waterproof protective layer. Apart from the discharge polarization tests on the CHI 760E work station, the galvanostatic discharge curves and discharge-charge curves were obtained on a LAND CT2001A (Wuhan

Jinnuo Electronics Co., Ltd., China).

## 3. Results and discussion

### 3.1. Syntheses and material features of TCNE-CTP and HNPC materials

A cyano-rich monomer TCNE with a high N content is innovatively applied to synthesize TCNE-CTP (Table S1). As depicted in Fig. 1a, TCNE-CTP is synthesized via the typical  $\text{ZnCl}_2$  ionothermal method at 400 °C for 72 h. Afterward, the  $\text{ZnCl}_2$  is removed by extensive washing with 1 M HCl and a large amount of water. The obtained TCNE-CTP then serves as the precursor to prepare the N-doped porous carbon materials by varying the activation temperatures from 700 to 1000 °C in the presence of KOH under inert atmosphere. The resulting HNPC materials are labeled according to the activation temperature (e.g., HNPC-700, HNPC-800, HNPC-900, and HNPC-1000).

The Fourier transform infrared spectroscopy (FT-IR) spectra of TCNE, TCNE-CTP, and HNPC materials are shown in Fig. 1b. The stretching vibration at 2220  $\text{cm}^{-1}$  of TCNE can be assigned to the conjugated nitriles. The new vibrational peaks appeared at around 1590 and 1180  $\text{cm}^{-1}$  in TCNE-CTP as compared with the TCNE monomer illustrate the existence of triazine fragments, suggesting the successful cyclotrimerization of cyano units in TCNE. Meanwhile, no stretching vibration of the conjugated nitrile is observed in TCNE-CTP, implying the complete transformation of the conjugated nitrile in TCNE. The signal of vibrational peak at 1590  $\text{cm}^{-1}$  gradually decreases in HNPC materials and even disappears in HNPC-1000, indicating the decomposition of triazine fragments along with activation process. The powder X-ray diffraction (PXRD) patterns of the TCNE-CTP and HNPC materials (Fig. S1) show a broad diffraction peak at about 22°–26° assigned to (001) reflection, suggesting the “graphitic” layer stacking within these materials [37].

The porosity of HNPC materials is characterized and shown in Table S2. The nitrogen adsorption-desorption isotherms show that the  $S_{\text{BET}}$  of TCNE-CTP is only 30  $\text{m}^2 \text{g}^{-1}$ , and the low  $S_{\text{BET}}$  is probably because the ultramicropore within TCNE-CTP confirmed by  $\text{CO}_2$  adsorption test (Fig. S2). In the activation process, C element in TCNE-CTP reacts with KOH to generate  $\text{K}_2\text{CO}_3$  and  $\text{CO}_2$ , creating pores in the dense skeleton and making further rearrangement reactions at the high temperature. As expected, the nitrogen adsorption-desorption isotherms of HNPC materials change from type I to type IV as the activation temperatures raised from 700 to 1000 °C, revealing that the micropores are successfully formed at 700 °C and then evolved into mesopores simultaneously with the increase in temperature above 800 °C (Fig. 1c). Specifically, the  $S_{\text{BET}}$  values of HNPC materials increase as the activation temperature rises, until reaching the highest  $S_{\text{BET}}$  value of 3210  $\text{m}^2 \text{g}^{-1}$  at 900 °C among HNPC materials (Fig. S3). The reduction of  $S_{\text{BET}}$  (2220  $\text{m}^2 \text{g}^{-1}$ ) for HNPC-1000 as compared with HNPC-900 may be interpreted as the decrease in percentage of micropores due to the considerable loss of C and N elements at a high activation temperature. The pore size distribution of HNPC materials is analyzed by the non-local-density functional theory model, confirming the generation of micropores and mesopores within HNPC network (Fig. 1d). It should be mentioned that pore volumes of TCNE-CTP and HNPC-700 are only 0.03 and 0.60  $\text{cm}^3 \text{g}^{-1}$ , respectively. Interestingly, the pore volumes enlarge to 1.95, 2.40, and 1.78  $\text{cm}^3 \text{g}^{-1}$  for HNPC-800, HNPC-900, and HNPC-1000, respectively (Fig. S4 and Table S2).

Scanning electron microscopy (SEM) images exhibit HNPC materials consist of irregular particles with a size ranging from several micrometers to dozens of micrometers (Fig. S5). The high-resolution transmission electron microscopy (HRTEM) image indicates the partially ordered structure of HNPC-900 (Fig. 1e and Fig. S6). As shown in Fig. 1f, elemental mapping images of HNPC-900 shows the homogeneous distribution of C and N elements.

The N contents of HNPC materials were confirmed by the measurements of element analysis (EA). The N content of TCNE-CTP is highly up



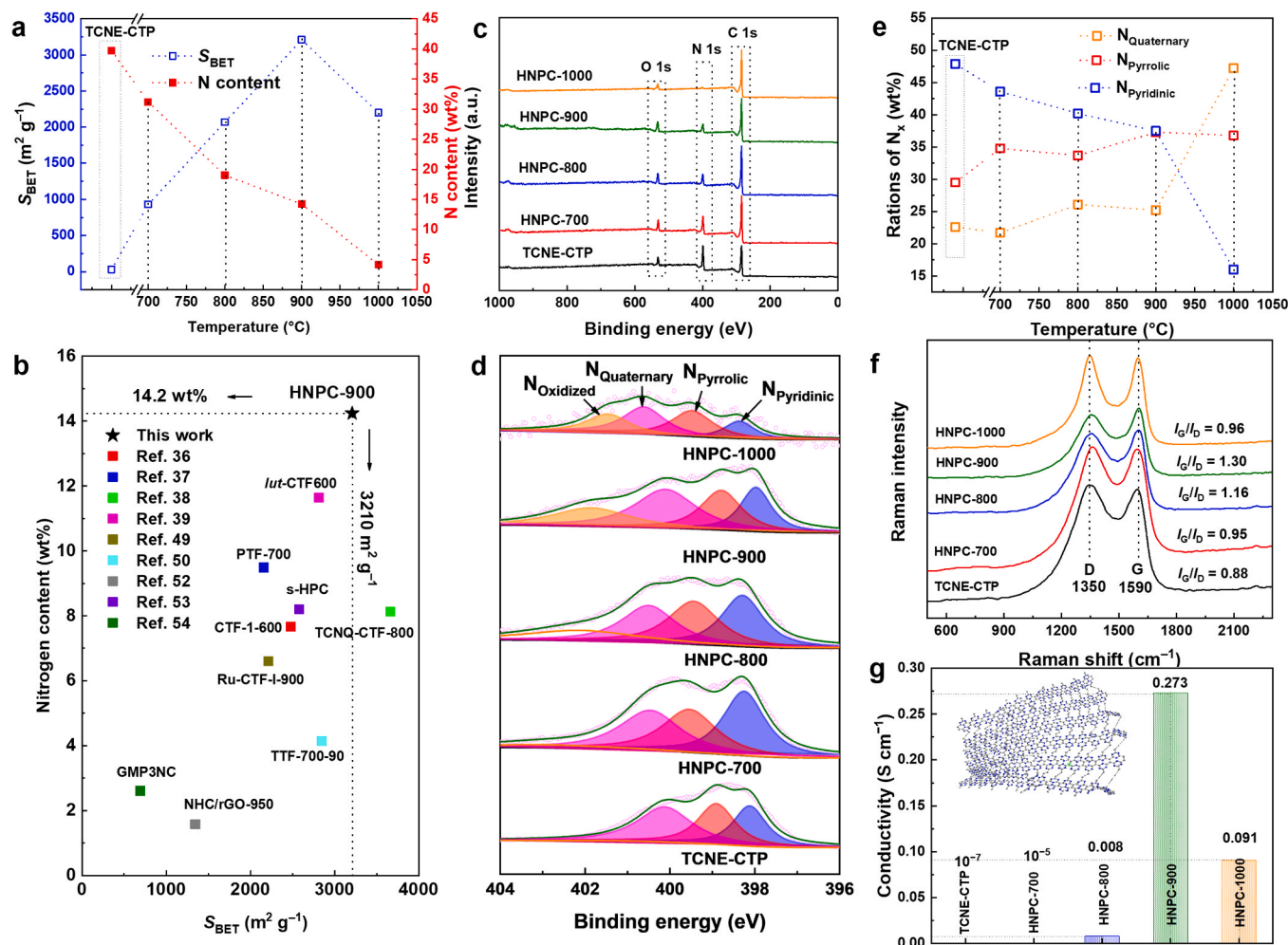


**Fig. 2.** (a) Specific surface areas (from BET calculation) and N contents (from elemental analysis) of TCNE-CTP and HNPC materials. (b) Comparison of  $S_{\text{BET}}$  and N content of HNPC-900 with relative reported materials. (c) XPS spectra of TCNE-CTP and HNPC materials. (d) The N 1s XPS spectra of HNPC materials. (e) The content variation of three kinds of N centers in HNPC materials. (f) Raman spectra and the  $I_G/I_D$  ratios of HNPC materials. (g) Electrical conductivities of HNPC materials.

to 39.7 wt%, which is comparable with theoretical N content (43.7 %) of TCNE-CTP, indicating the limited loss of N content during the preparation of TCNE-CTP (Table S3). Although the N contents of HNPC materials inevitably decrease with the etching of C element by KOH during activation process, HNPC-900 with  $S_{\text{BET}}$  of  $3210 \text{ m}^2 \text{ g}^{-1}$  still possesses a high level of 14.2 wt% N (Fig. 2a). To the best of our knowledge, the porous carbon material with both such high  $S_{\text{BET}}$  ( $3210 \text{ m}^2 \text{ g}^{-1}$ ) and high N content (14.2 wt%) has not been reported. As compared with other POP-derived N-doped porous carbon materials (Fig. 2b) [36–39,49,50–54], HNPC-900 exhibits the highest N content and prominent  $S_{\text{BET}}$ , implying that HNPC-900 can provide a high concentration of active sites and a large accessible surface area for adsorption and catalytic reactions.

X-ray photoelectron spectroscopy (XPS) measurement was employed to study the evolution of N configurations. The contents of C and N elements of HNPC materials from XPS measurements are nearly consistent with the results of element analysis (Fig. 2c and Fig. S7). As shown in Fig. 2d and Fig. S8, N 1s XPS spectra of HNPC materials can be categorized as  $N_{\text{Pyridinic}}$ ,  $N_{\text{Pyrrolic}}$ ,  $N_{\text{Quaternary}}$ , and  $N_{\text{Oxidized}}$  species, and C 1s XPS spectra of HNPC materials are classified as  $C_{\text{Pyridinic}}$  and  $C_{\text{Vinyl}}$  (Table S4). The  $N_{\text{Oxidized}}$  species is caused by the combination of N and  $\text{O}_2$  during the measurement. The reversible cyclotrimerization reaction of cyano units contributes to the existence of  $N_{\text{Pyridinic}}$  and  $N_{\text{Pyrrolic}}$  species situated at 398.3 and 399.6 eV, respectively. The  $N_{\text{Quaternary}}$  species at about 400.8 eV is derived from the aromatic structures. As shown in Fig. 2e, the contents of  $N_{\text{Pyridinic}}$ ,  $N_{\text{Pyrrolic}}$ , and  $N_{\text{Quaternary}}$

species were plotted as a function of activation temperatures. The content of  $N_{\text{Pyridinic}}$  (47.9 wt%) is obviously higher than those of  $N_{\text{Pyrrolic}}$  (29.5 wt%) and  $N_{\text{Quaternary}}$  (22.6 wt%) for TCNE-CTP, illustrating that  $N_{\text{Pyridinic}}$  from triazine fragments is the main N species in TCNE-CTP. However, triazine fragments slowly decompose along with the rise of activation temperature, causing the loss of  $N_{\text{Pyridinic}}$  during the activation process. Conventionally, HNPC-900 shows the contents of 25.2 wt %, 37.3 wt %, and 37.5 wt % for  $N_{\text{Pyridinic}}$ ,  $N_{\text{Pyrrolic}}$ , and  $N_{\text{Quaternary}}$ , respectively. When the activation temperature was up to  $1000^\circ\text{C}$ , the corresponding product HNPC-1000 shows a sudden decrease in N content, in which  $N_{\text{Pyridinic}}$  content (16.0 wt%) is far below HNPC-900 (37.5 wt%). Numerous studies have shown that N atoms have promising electrocatalytic activity in some electrocatalysis reactions [55,56], indicating the electrocatalysis application of HNPC materials.

Raman spectra of HNPC materials exhibit broad defective (D) and graphitic (G) bands at  $1350$  and  $1590 \text{ cm}^{-1}$  (Fig. 2f). The intensity ratio of G and D bands ( $I_G/I_D$ ) increases from 0.95 to 1.30 as the activation temperature increases from  $700$  to  $900^\circ\text{C}$ . The improvement of ordered structure is beneficial to enhance electrical conductivity of HNPC materials. As displayed in Fig. 2g, the electrical conductivity of HNPC-900 is as high as  $0.2730 \text{ S cm}^{-1}$ , which is an improvement of 37 times over  $0.0072 \text{ S cm}^{-1}$  of the tetracyanoquinodimethane-based CTF [38]. The high inherent conductivity of HNPC-900 can eliminate the Schottky energy barriers on the interface of catalyst–electrolyte, thus enhancing catalytic activity and ensuring high energy conversion efficiency [57,



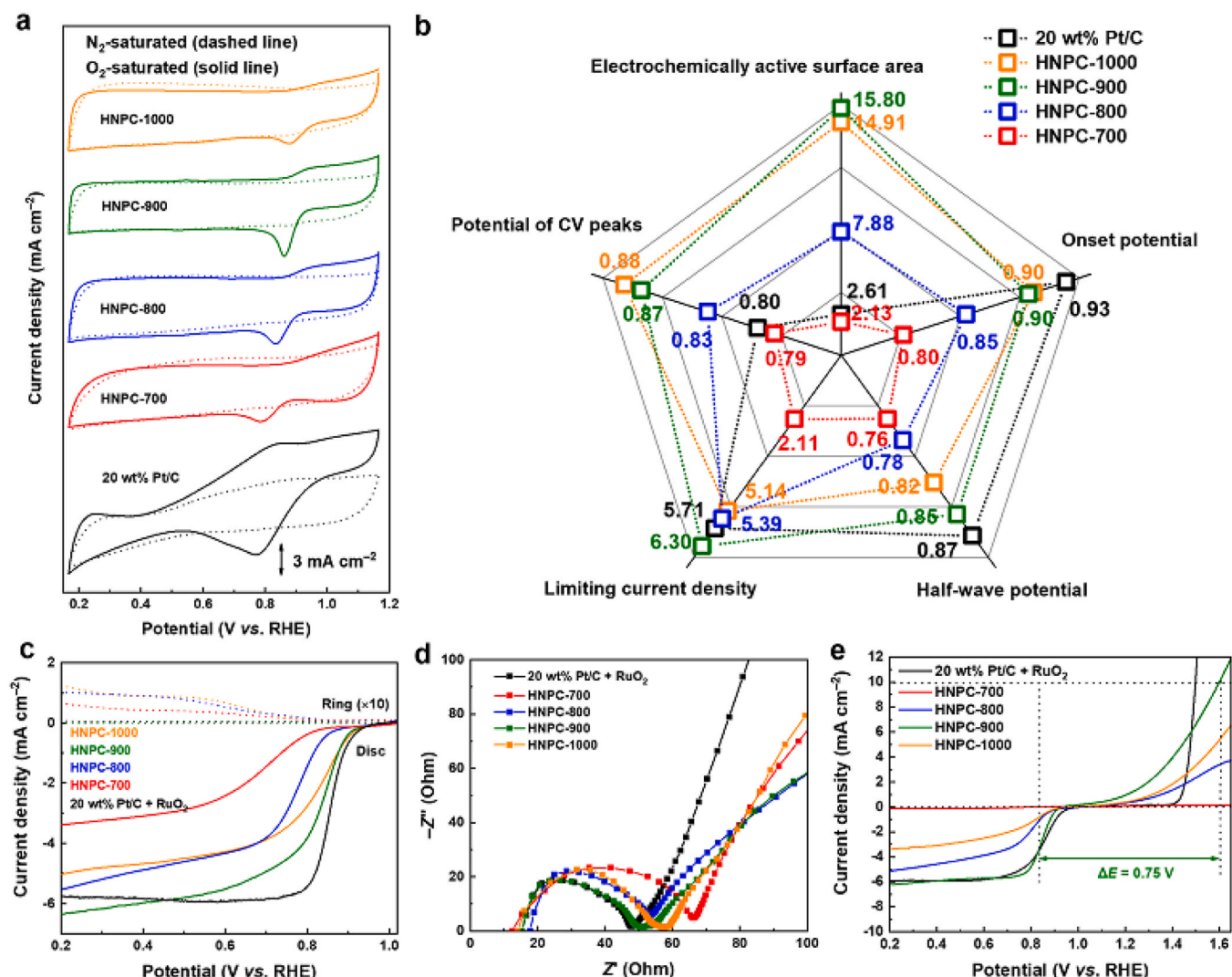


**Fig. 3.** (a) CV curves of HNPC materials and 20 wt% Pt/C in  $N_2$ -saturated or  $O_2$ -saturated 0.1 M KOH electrolyte solution. (b) Comparison of potential of CV peaks, onset potential, half-wave potential, limiting current density, and electrochemical activity surface area for 20 wt% Pt/C and HNPC materials. (c) LSV curves of 20 wt% Pt/C and HNPC materials at 1600 rpm in  $O_2$ -saturated 0.1 M KOH solution using RRDE. (d) Nyquist plots of HNPC materials and 20 wt% Pt/C +  $RuO_2$  electrocatalyst on the rotating disk electrode in 0.1 M KOH electrolyte solution. (e) LSV curves of HNPC materials and 20 wt% Pt/C +  $RuO_2$  electrocatalyst in  $O_2$ -saturated 0.1 M KOH electrolyte solution at 1600 rpm.

[58].

### 3.2. HNPC materials as bifunctional electrocatalysts towards ORR and OER

Considering the large  $S_{BET}$ , high N content, and excellent electrical conductivity of HNPC materials, their electrocatalytic performances towards ORR were evaluated through CV, LSV, and long-term electrocatalytic stability tests. In the CV tests, no peak is observed when HNPC materials were employed as the electrocatalysts in an  $N_2$ -saturated 0.1 M KOH electrolyte solution (dashed lines in Fig. 3a). Inversely, the characteristic cathodic peaks occurred in an  $O_2$ -saturated electrolyte solution (solid lines), indicating that HNPC materials possess catalytic abilities towards the ORR. In addition, with the increase in activation temperature, the corresponding HNPC material shows a gradually shifted reduction potential towards positive voltage, suggesting the enhanced electrocatalytic activity. Fig. S9 shows the LSV curves of HNPC materials at a rotating speed of 1600 rpm in 0.1 M KOH electrolyte solution. The onset potential and half-wave potential of HNPC materials gradually improve with activation temperature. Both HNPC-900 and HNPC-1000 show relatively high onset potential of 0.90 V vs.

reversible hydrogen electrode (RHE), which is slightly lower than that of commercial 20 wt% Pt/C catalyst (0.93 V) (Fig. S10). The half-wave potential of HNPC-900 is 0.85 V, which is better than those of the reported POP-based electrocatalysts (Table S5) and even comparable to 20 wt% Pt/C (0.87 V). Notably, the limiting current density of HNPC-900 is 6.3 mA cm<sup>-2</sup>, which is obviously superior to HNPC-700 (2.1 mA cm<sup>-2</sup>), HNPC-800 (5.4 mA cm<sup>-2</sup>), HNPC-1000 (5.1 mA cm<sup>-2</sup>), and 20 wt% Pt/C (5.7 mA cm<sup>-2</sup>). Our result confirms to the quaternary N and pyridinic N contribute to the limiting current density and the onset potential for the ORR, respectively [59,60]. Thus, HNPC-900 with large  $S_{BET}$ , high electrical conductivity, and abundant quaternary N and pyridinic N possesses the highest onset potential, the highest half-wave potential, and the highest limiting current density among these HNPC materials (Fig. 3b). As shown in Fig. S11, the limiting current densities of HNPC materials increase with the elevated rotating speed by virtue of the shortened diffusion distance. This increase in the limiting current density was plotted in terms of associated Koutecky-Levich (K-L) plots. The linear increases in  $j^{-1}$  versus the  $\omega^{-1/2}$  for HNPC materials illustrate a first-order reaction with respect to the dissolved  $O_2$  [61].

For ORR, the electron transfer process via four-electron reaction pathway is favor to carry out a high-power density. The electron transfer

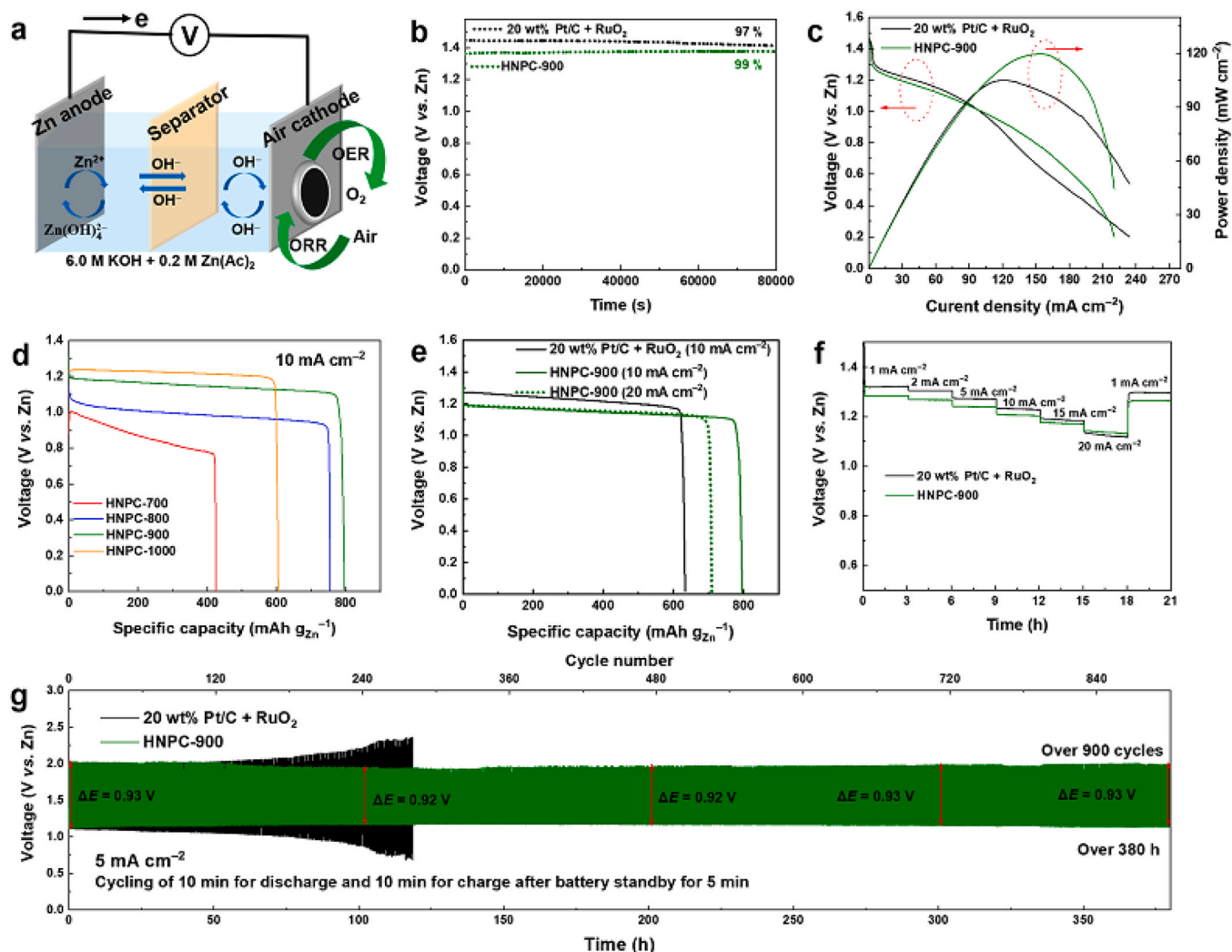


**Fig. 4.** (a) Schematic illustration of a zinc-air battery. (b) Open circuit voltage curves of as-fabricated ZABs based on HNPC-900 or 20 wt% Pt/C + RuO<sub>2</sub> air-cathode. (c) Discharge polarization curves and the corresponding power density plots of HNPC-900 and 20 wt% Pt/C + RuO<sub>2</sub>. (d) Galvanostatic discharge curves of HNPC materials at 10 mA cm<sup>-2</sup>. (e) Galvanostatic discharge curves of HNPC-900 at 10 and 20 mA cm<sup>-2</sup> and 20 wt% Pt/C + RuO<sub>2</sub> at 10 mA cm<sup>-2</sup>. (f) Rate performances of HNPC-900 and 20 wt% Pt/C + RuO<sub>2</sub> at 1, 2, 5, 10, 15, 20, and 1 mA cm<sup>-2</sup>. (g) Discharge-charge curves of HNPC-900 and 20 wt% Pt/C + RuO<sub>2</sub> at 5 mA cm<sup>-2</sup> by discharging for 10 min and charging for 10 min.

number  $n$  and H<sub>2</sub>O<sub>2</sub> yield are determined by RRDE tests. The  $n$  value (3.97–3.99) of HNPC-900 is very close to 4.0, and the H<sub>2</sub>O<sub>2</sub> yield is less than 1.50 %, confirming that HNPC-900 possesses a four-electron reaction pathway with relatively limited coproducts and high selectivity towards the product (OH<sup>-</sup>) of the four-electron reaction pathway (Fig. 3c and Fig. S12). Furthermore, the long-term stability of HNPC-900 is superior to HNPC-800, HNPC-1000, and 20 wt% Pt/C (Fig. S13), indicating the excellent electrocatalytic activity of HNPC-900 for ORR.

The electrocatalytic performances of HNPC materials for OER were conducted in 0.1 M KOH electrolyte solution, and the RuO<sub>2</sub> is employed as a reference substance [33,62–64]. The measured potential of HNPC-900 at the current density of 10 mA cm<sup>-2</sup> ( $E_{j=10}$ ) is 1.60 V vs. RHE, which is much smaller than those of other HNPC materials and comparable to that of RuO<sub>2</sub> (1.54 V vs. RHE), indicating the good electrocatalytic activity of HNPC-900 for OER (Fig. S14). Furthermore, the OER performance of HNPC-900 is superior to the reported electrocatalysts based on the POPs (Table S6). The doped N atoms improve the charge mobility of the carbon matrix by playing the role of electron-donor so that enhance the catalytic activity of carbon matrix for electron-transfer reactions [65]. Furthermore, the doped N atoms are favorable to fast adsorption and exchange of reactants and reaction intermediates throughout the OER process, such as O<sub>2</sub>, OH<sup>-</sup>, and H<sub>2</sub>O

species [66]. The charge transfer resistances ( $R_{ct}$ ) of HNPC materials are comparable to that of the RuO<sub>2</sub>, indicating the fast reaction kinetics of HNPC materials for OER by virtue of high conductivity (Fig. 3d). CV tests are further performed to examine the electrochemical double-layer capacitance ( $C_{dl}$ ) and the intrinsic electrocatalytic activity of HNPC materials (Fig. S15). Among these HNPC materials, HNPC-900 possesses the highest  $C_{dl}$  (15.80 mF cm<sup>-2</sup>) (Fig. S16), illustrating the largest electrochemically active surface area (ECSA) of HNPC-900 for OER. A negligible decrease in current was observed from the result of continuous chronoamperometry test at potential of 1.50 V vs. RHE for more than 25,000 s (Fig. S17), suggesting the good long-term stability of HNPC-900.

The bifunctional electrocatalytic activity of HNPC materials towards ORR and OER can be assessed by the value of the potential gap  $\Delta E$  ( $\Delta E = E_{j=10} - E_{half-wave}$ ). As shown in Fig. 3e, HNPC-900 possesses a small  $\Delta E$  value of 0.75 V, which is superior to those of the most reported bifunctional electrocatalysts (Table S7). To explore the influence of OER measurement on ORR catalytic activity, the LSV curve of HNPC-900 for ORR after the OER test is shown in Fig. S18. The half-wave potential of HNPC-900 shows a minimal negative shift of only 7 mV as compared with the initial half-wave potential, further confirming the excellent bifunctional electrocatalytic activity of HNPC-900, which may be a

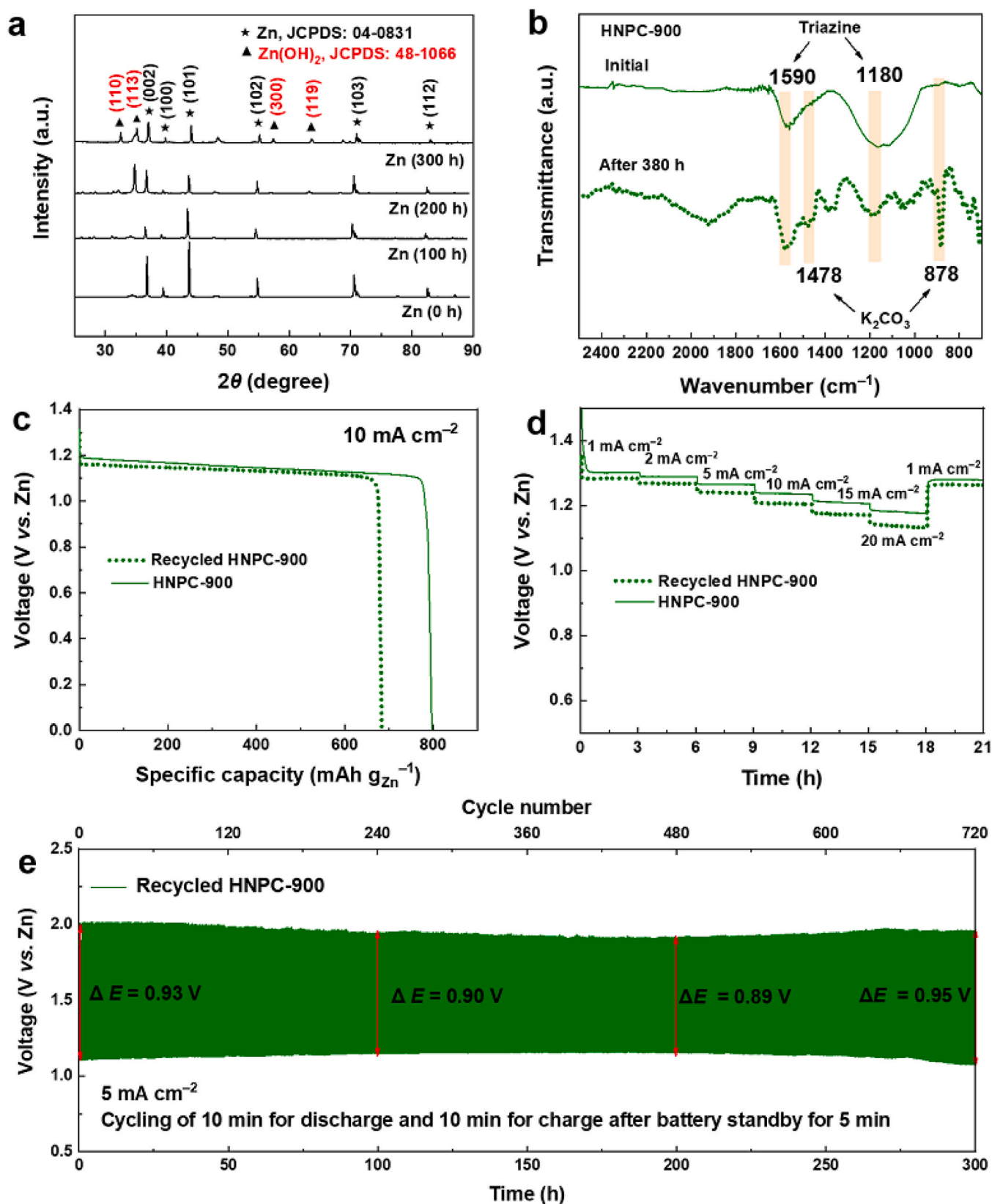


**Fig. 5.** (a) PXRD characterizations of the recycled zinc plate. (b) FT-IR curves of initial and recycled HNPC-900. (c) The galvanostatic discharge curves of ZABs based on initial and recycled HNPC-900 at  $10 \text{ mA cm}^{-2}$ . (d) The galvanostatic discharge curves of ZABs based on initial and recycled HNPC-900 at 1, 2, 5, 10, 15, 20, and 1  $\text{mA cm}^{-2}$ . (e) Discharge–charge curves at  $5 \text{ mA cm}^{-2}$  with discharge for 10 min and charge for 10 min after standby for 5 min.



promising bifunctional electrocatalyst for ZABs.

### 3.3. Performance demonstration in zinc–air batteries

The performances of HNPC materials in ZABs are investigated by employing the homemade batteries with Zn plate as the anode, carbon paper coated with HNPC materials as air cathode, and a mixture of aqueous KOH solution (6.0 M) and aqueous  $\text{Zn}(\text{Ac})_2$  solution (0.2 M) as the electrolyte solution (Fig. 4a). The composite of 20 wt% Pt/C and  $\text{RuO}_2$  (named as 20 wt% Pt/C +  $\text{RuO}_2$ ) is applied as a bifunctional material to prepare the reference air cathode. The open-circuit voltage (OCV) of the ZAB fabricated by HNPC-900 is up to 1.37 V and a negligible change of only 0.95 % after 80,000 s was observed (Fig. 4b). In addition, HNPC-900 shows a current density of  $220 \text{ mA cm}^{-2}$  and a peak power density of  $120 \text{ mW cm}^{-2}$  (Fig. 4c), which are comparable to  $240 \text{ mA cm}^{-2}$  and  $100 \text{ mW cm}^{-2}$  for 20 wt% Pt/C +  $\text{RuO}_2$  and superior to other HNPC materials (Fig. S19).

The galvanostatic discharge curves and cycling stability of HNPC materials were explored to further evaluate their practical electrocatalytic performances. As shown in Fig. 4d, HNPC-900 shows the highest specific capacity of  $797 \text{ mAh g}_{\text{Zn}}^{-1}$  at  $10 \text{ mA cm}^{-2}$  as compared with HNPC-700 ( $425 \text{ mAh g}_{\text{Zn}}^{-1}$ ), HNPC-800 ( $756 \text{ mAh g}_{\text{Zn}}^{-1}$ ), and HNPC-1000 ( $604 \text{ mAh g}_{\text{Zn}}^{-1}$ ). Even at a high current density of  $20 \text{ mA cm}^{-2}$ , HNPC-900 still possesses a high specific capacity of  $705 \text{ mAh g}_{\text{Zn}}^{-1}$  (Fig. 4e). The galvanostatic discharging tests at various consecutive current densities were conducted to evaluate the rate performances of ZABs based on HNPC-900. As shown in Fig. 4f, HNPC-900 cathode displays an initial discharge voltage of 1.37 V at  $1 \text{ mA cm}^{-2}$  and maintains stable discharge voltages at different current densities of 1, 2, 5, 10, 15, and  $20 \text{ mA cm}^{-2}$  with each current density for 3 h. The discharge voltage at  $20 \text{ mA cm}^{-2}$  for HNPC-900 cathode is even higher than that of 20 wt% Pt/C +  $\text{RuO}_2$  cathode. Notably, the discharge voltage for HNPC-900 cathode can be well-recovered to around 1.37 V when the current density restored to  $1 \text{ mA cm}^{-2}$ , illustrating a good rate performance of HNPC-900 cathode owing to the favorable pathways for mass-transfer by virtue of high porosity. In contrast, other HNPC materials show inefficient rate performances due to the low specific capacity (Fig. S20).

The cycling stability of HNPC-900 cathode was measured by the continuous galvanostatic discharge–charge at  $5 \text{ mA cm}^{-2}$  (Fig. 4g). HNPC-900 cathode shows limited voltage fluctuations for more than 380 h (960 cycles), indicating that HNPC-900 cathode possesses the highly stable rechargeability. A low voltage gap (0.93 V) is achieved for HNPC-900 cathode after 380 h (960 cycles) cycling test, suggesting an outstanding cycling stability of HNPC-900 cathode. In contrast, contrastive cathode in Fig. 4g shows an inferior cycling stability with obvious deterioration during the long-term cycling tests. Moreover, the ZABs based on HNPC-900 cathode are obviously competitive in specific capacity and durability as compared with the reported bifunctional electrocatalysts (Table S8), confirming HNPC-900 can be regarded as a promising bifunctional electrocatalyst for high-performance ZABs.

### 3.4. Recyclable air cathode

The failure mechanism of the ZABs based on HNPC-900 is investigated to increase the service life. It is known that the Zn plate will be inevitably corroded by the alkaline electrolyte solution after continuous circulation. As observed by SEM imaging, the surface of the recycled Zn plate has become rough and is covered by Zn dendrites (Figs. S21 and S22). PXRD patterns of the recycled zinc plate confirm the formation of zinc hydroxide (JCPDS: 48-1066) on the surface of the Zn plate (Fig. 5a), resulting in the efficacy loss of Zn anode [67]. In addition, the deterioration of the electrolyte solution caused by the acidic gas carbon dioxide ( $\text{CO}_2$ ) in air and the coproducts deposited on the electrocatalyst surface further lead to the fading performance of the ZABs [68]. As confirmed by the FT-IR and energy dispersive X-ray spectrometry (EDS), the surface of HNPC-900 is covered by the coproduct potassium carbonate (Fig. 5b and

Fig. S23) [69], which may block the transport paths, cover the active sites, and decrease the conductivity of HNPC-900.

The recyclable ZABs were assembled by replacing the corroded zinc plate and the metamorphic electrolyte solution, and washing HNPC-900 cathode with 0.01 M HCl solution and water to remove the coproducts. It should be noted that recyclable strategy here may be suitable for the metal-free electrocatalysts but not for the metal-based electrocatalysts due to their possible destroy by the acid cleaning process. The performances of the recyclable ZABs were then measured and compared with the initial batteries. According to the galvanostatic discharge curves (Fig. 5c), the recyclable ZAB based on HNPC-900 possesses a specific capacity of  $690 \text{ mAh g}_{\text{Zn}}^{-1}$  at  $10 \text{ mA cm}^{-2}$ , which is 86.6 % of the initial battery. Furthermore, the recyclable ZAB still shows a good rate performance despite a few decreases in voltage (Fig. 5d), implying the retention of most active sites within the recycled HNPC-900. More importantly, the recyclable ZAB shows good long-term stability for more than 300 h (720 cycles) (Fig. 5e). The above results demonstrate the fading performance of the ZABs based on HNPC-900 cathode is mainly caused from zinc plate corrosion, rather than the degradation of the intrinsic catalytic performance of HNPC-900, indicating the high stability of HNPC-900. The superb performance of HNPC-900 cathode can be ascribed to the high N content, large  $S_{\text{BET}}$ , and high electrical conductivity, which afford sufficient active sites for electrocatalytic reactions, and promote effective electron and mass transport in ZABs.

## 4. Conclusions

In summary, we developed a covalent triazine polymer (TCNE-CTP) with 39.7 wt% N content by cyclotrimerization of the tetracyanoethylene monomer. TCNE-CTP-derived N-doped porous carbon (HNPC-900) possesses a large  $S_{\text{BET}}$  ( $3210 \text{ m}^2 \text{ g}^{-1}$ ), high electrical conductivity ( $0.273 \text{ S cm}^{-1}$ ), and high N content (14.2 wt%). As an air-cathode for ZABs, HNPC-900 cathode delivers excellent performance for ZABs with a high specific capacity ( $797 \text{ mAh g}_{\text{Zn}}^{-1}$ ) and stable rechargeability (more than 380 h over 960 cycles at  $5 \text{ mA cm}^{-2}$ ) by virtue of the bifunctional electrocatalytic activity for ORR and OER. The outstanding performance of HNPC-900 for ZABs is ascribed to high electronic conductivity, large  $S_{\text{BET}}$ , and sufficient electrocatalytic sites provided by the high N content. This work not only provides meaningful guidance for designing and developing high N-doped porous carbon materials, but also offers an inspiration of applying the high N-doped porous carbon materials in various advanced energy-related fields.

### CRedit authorship contribution statement

**You Tao:** Conceptualization, Investigation, Validation, Writing – original draft. **Dong-Hui Yang:** Conceptualization, Writing – review & editing, Supervision. **Hui-Yuan Kong:** Conceptualization, Methodology, Investigation. **Tian-Xiong Wang:** Validation, Data curation. **Zihao Li:** Formal analysis, Data curation. **Xuesong Ding:** Supervision, Project administration, Funding acquisition. **Bao-Hang Han:** Supervision, Project administration, Funding acquisition, Conceptualization, Writing – review & editing.

### Declaration of Competing Interest

The authors declare that they have no known competing financial interests or personal relationships that could have appeared to influence the work reported in this paper.

### Data availability

Data will be made available on request.

## Acknowledgements

The financial support of the National Natural Science Foundation of China (Grants 22161132010, 22075060, and 22171057), the Strategic Priority Research Program of Chinese Academy of Sciences (Grant XDB36000000), and the National Key R&D Program of Ministry of Science and Technology of China (Grant 2022YFE0101800) is acknowledged.

## Appendix A. Supporting information

Supplementary data associated with this article can be found in the online version at [doi:10.1016/j.apcatb.2023.123088](https://doi.org/10.1016/j.apcatb.2023.123088).

## References

- [1] H. Wang, Y. Shao, S. Mei, Y. Lu, M. Zhang, J.-K. Sun, K. Matyjaszewski, M. Antonietti, J. Yuan, Polymer-derived heteroatom-doped porous carbon materials, *Chem. Rev.* 120 (2020) 9363–9419, <https://doi.org/10.1021/acs.chemrev.0c00080>.
- [2] T.-Y. Ma, L. Liu, Z.-Y. Yuan, Direct synthesis of ordered mesoporous carbons, *Chem. Soc. Rev.* 42 (2013) 3977–4003, <https://doi.org/10.1039/C2CS35301F>.
- [3] M. He, Y. Sun, B. Han, Green carbon science: efficient carbon resource processing, utilization, and recycling towards carbon neutrality, *Angew. Chem., Int. Ed.* 61 (2022), e202112835, <https://doi.org/10.1002/anie.202112835>.
- [4] H. Jiang, J. Xia, L. Jiao, X. Meng, P. Wang, C.-S. Lee, W. Zhang, Ni single atoms anchored on N-doped carbon nanosheets as bifunctional electrocatalysts for urea-assisted rechargeable Zn–air batteries, *Appl. Catal. B Environ.* 310 (2022), 121352, <https://doi.org/10.1016/j.apcatb.2022.121352>.
- [5] S. Wang, H. Wang, C. Huang, P. Ye, X. Luo, J. Ning, Y. Zhong, Y. Hu, Trifunctional electrocatalyst of N-doped graphitic carbon nanosheets encapsulated with CoFe alloy nanocrystals: the key roles of bimetal components and high-content graphitic-N, *Appl. Catal. B Environ.* 298 (2021), 120512, <https://doi.org/10.1016/j.apcatb.2021.120512>.
- [6] K. Gong, F. Du, Z. Xia, M. Durstock, L. Dai, Nitrogen-doped carbon nanotube arrays with high electrocatalytic activity for oxygen reduction, *Science* 323 (2009) 760–764, <https://doi.org/10.1126/science.1168049>.
- [7] D. Guo, R. Shibuya, C. Akiba, S. Saji, T. Kondo, J. Nakamura, Active sites of nitrogen-doped carbon materials for oxygen reduction reaction clarified using model catalysts, *Science* 351 (2016) 361–365, <https://doi.org/10.1126/science.1240832>.
- [8] X. Xiao, X. Li, Z. Wang, G. Yan, H. Guo, Q. Hu, L. Li, Y. Liu, J. Wang, Robust template-activated cooperated pyrolysis enabling hierarchically porous honeycombed defective carbon as highly-efficient metal-free bifunctional electrocatalyst for Zn-air batteries, *Appl. Catal. B Environ.* 265 (2020), 118603, <https://doi.org/10.1016/j.apcatb.2020.118603>.
- [9] H. Zoua, G. Li, L. Duan, Z. Kou, J. Wang, In situ coupled amorphous cobalt nitride with nitrogen-doped graphene aerogel as a trifunctional electrocatalyst towards Zn-air battery driven full water splitting, *Appl. Catal. B Environ.* 259 (2019), 118100, <https://doi.org/10.1016/j.apcatb.2019.118100>.
- [10] H.B. Yang, J. Miao, S.-F. Hung, J. Chen, H.B. Tao, X. Wang, L. Zhang, R. Chen, J. Gao, H.M. Chen, L. Dai, B. Liu, Identification of catalytic sites for oxygen reduction and oxygen evolution in N-doped graphene materials: development of highly efficient metal-free bifunctional electrocatalyst, *Sci. Adv.* 2 (2016), e1501122, <https://doi.org/10.1126/sciadv.1501122>.
- [11] W.-J. Liu, W.-W. Li, H. Jiang, H.-Q. Yu, Fates of chemical elements in biomass during its pyrolysis, *Chem. Rev.* 117 (2017) 6367–6398, <https://doi.org/10.1021/acs.chemrev.6b00647>.
- [12] H. Jiang, J. Gu, X. Zheng, M. Liu, X. Qiu, L. Wang, W. Li, Z. Chen, X. Ji, J. Li, Defect-rich and ultrathin N-doped carbon nanosheets as advanced trifunctional metal-free electrocatalysts for the ORR, OER, and HER, *Energy Environ. Sci.* 12 (2019) 322–333, <https://doi.org/10.1039/c8ee03276a>.
- [13] Q. Lai, J. Zheng, Z. Tang, D. Bi, J. Zhao, Y. Liang, Optimal configuration of N-doped carbon defects in 2D turbostratic carbon nanomesh for advanced oxygen reduction electrocatalysis, *Angew. Chem., Int. Ed.* 59 (2020) 11999–12006, <https://doi.org/10.1002/anie.202000936>.
- [14] C. Liu, F. Liu, H. Li, J. Chen, J. Fei, Z. Yu, Z. Yuan, C. Wang, H. Zheng, Z. Liu, M. Xu, G. Henkelman, L. Wei, Y. Chen, One-dimensional van der Waals heterostructures as efficient metal-free oxygen electrocatalysts, *ACS Nano* 15 (2021) 3309–3319, <https://doi.org/10.1002/acs.nano.010242>.
- [15] P. Li, H. Wang, X. Tan, W. Hu, M. Huang, J. Shi, J. Chen, S. Liu, Z. Shi, Z. Li, Bifunctional electrocatalyst with CoN<sub>3</sub> active sites dispersed on N-doped graphitic carbon nanosheets for ultrafast Zn–air batteries, *Appl. Catal. B Environ.* 316 (2022), 121674, <https://doi.org/10.1016/j.apcatb.2022.121674>.
- [16] C. Hu, L. Dai, Doping of carbon materials for metal-free electrocatalysis, *Adv. Mater.* 31 (2019), 1804672, <https://doi.org/10.1002/adma.201804672>.
- [17] Y. Zang, C. Mi, R. Wang, H. Chen, P. Peng, Z. Xiang, S. Zang, T.C.W. Mak, Pyrolysis-free synthesized catalyst towards acidic oxygen reduction by deprotonation, *Angew. Chem., Int. Ed.* 60 (2021) 20865–20871, <https://doi.org/10.1002/anie.202106661>.
- [18] H.-W. Liang, X. Zhuang, S. Brüller, X. Feng, K. Müllen, Hierarchically porous carbons with optimized nitrogen-doping as highly active electrocatalysts for oxygen reduction, *Nat. Commun.* 5 (2014) 4973, <https://doi.org/10.1038/ncomms5973>.
- [19] A. Pramanik, H.S. Kang, Density functional theory study of O<sub>2</sub> and NO adsorption on heteroatom-doped graphenes including the van der Waals interaction, *J. Phys. Chem. C* 115 (2011) 10971–10978, <https://doi.org/10.1021/jp200783b>.
- [20] D. Geng, Y. Chen, Y. Chen, Y. Li, R. Li, X. Sun, S. Ye, S. Knights, High oxygen-reduction activity and durability of nitrogen-doped graphene, *Energy Environ. Sci.* 4 (2011) 760–764, <https://doi.org/10.1039/C0EE00326C>.
- [21] Y. Yuan, I. Cabasso, H. Liu, Surface morphology of nanostructured polymer-based activated carbons, *J. Phys. Chem. B* 112 (2008) 14364–14372, <https://doi.org/10.1021/jp800771r>.
- [22] B. Adeniran, R. Mokaya, Low temperature synthesized carbon nanotube superstructures with superior CO<sub>2</sub> and hydrogen storage capacity, *J. Mater. Chem. A* 3 (2015) 5148–5161, <https://doi.org/10.1039/C4TA06539E>.
- [23] Y. Zhu, S. Murali, M.D. Stoller, K.J. Ganesh, W. Cai, P.J. Ferreira, A. Pirkle, R. M. Wallace, K.A. Cychosz, M. Thommes, D. Su, E.A. Stach, R.S. Ruoff, Carbon-based supercapacitors produced by activation of graphene, *Science* 332 (2011) 1537–1541, <https://doi.org/10.1126/science.1200770>.
- [24] E. Gottlieb, K. Matyjaszewski, T. Kowalewski, Polymer-based synthetic routes to carbon-based metal-free catalysts, *Adv. Mater.* 31 (2019), 1804626, <https://doi.org/10.1002/adma.201804626>.
- [25] X. Zhuang, F. Zhang, D. Wu, N. Forler, H. Liang, M. Wagner, D. Gehrig, M. R. Hansen, F. Laquai, X. Feng, Two-dimensional sandwich-type, graphene-based conjugated microporous polymers, *Angew. Chem., Int. Ed.* 52 (2013) 9668–9672, <https://doi.org/10.1002/anie.201304496>.
- [26] P. Mu, Z. Zhang, W. Bai, J. He, H. Sun, Z. Zhu, W. Liang, A. Li, Superwetting monolithic hollow-carbon-nanotubes aerogels with hierarchically nanoporous structure for efficient solar steam generation, *Adv. Energy Mater.* 9 (2019), 1802158, <https://doi.org/10.1002/aenm.201802158>.
- [27] Y. Liao, Z. Cheng, W. Zuo, A. Thomas, C.F.J. Faul, Nitrogen-rich conjugated microporous polymers: facile synthesis, efficient gas storage, and heterogeneous catalysis, *ACS Appl. Mater. Interfaces* 9 (2017) 38390–38400, <https://doi.org/10.1021/acsami.7b09553>.
- [28] T. Ben, Y. Li, L. Zhu, D. Zhang, D. Cao, Z. Xiang, X. Yao, S. Qiu, Selective adsorption of carbon dioxide by carbonized porous aromatic framework (PAF), *Energy Environ. Sci.* 5 (2012) 8370–8376, <https://doi.org/10.1039/C2EE21935B>.
- [29] Y. Dong, S. Das, L. Zhu, T. Ben, S. Qiu, Standout electrochemical performance of SnO<sub>2</sub> and Sn/SnO<sub>2</sub> nanoparticles embedded in a KOH activated carbonized porous aromatic framework (PAF-1) matrix as the anode for lithium-ion batteries, *J. Mater. Chem. A* 4 (2016) 18822–18831, <https://doi.org/10.1039/C6TA09384A>.
- [30] P. Peng, Z. Zhou, J. Guo, Z. Xiang, Well-defined 2D covalent organic polymers for energy electrocatalysis, *ACS Energy Lett.* 2 (2017) 1308–1314, <https://doi.org/10.1021/acsenenergylett.7b00267>.
- [31] K. Wang, L. Huang, S. Razzaque, S. Jin, B. Tan, Fabrication of hollow microporous carbon spheres from hyper-crosslinked microporous polymers, *Small* 12 (2016) 3134–3142, <https://doi.org/10.1002/sml.201600256>.
- [32] L. Zhao, P.-W. Xiao, Q. Chen, C. Fu, B.-H. Han, Polycarbazole and biomass-derived flexible nitrogen-doped porous carbon materials for gas adsorption and sensing, *J. Mater. Chem. A* 8 (2020) 6804–6811, <https://doi.org/10.1039/C9TA13910A>.
- [33] Y.-N. Sun, J. Yang, X. Ding, W. Ji, A. Jaworski, A. Hedin, B.-H. Han, Synergistic contribution of nitrogen and fluorine species in porous carbons as metal-free and bifunctional oxygen electrocatalysts for zinc–air batteries, *Appl. Catal. B Environ.* 297 (2021), 120448, <https://doi.org/10.1016/j.apcatb.2021.120448>.
- [34] J.-S.M. Lee, M.E. Briggs, T. Hasell, A.I. Cooper, Hyperporous carbons from hypercrosslinked polymers, *Adv. Mater.* 28 (2016) 9804–9810, <https://doi.org/10.1002/adma.201603051>.
- [35] P. Kuhn, M. Antonietti, A. Thomas, Porous, Covalent triazine-based frameworks prepared by ionothermal synthesis, *Angew. Chem., Int. Ed.* 47 (2008) 3450–3453, <https://doi.org/10.1002/anie.200705710>.
- [36] L. Hao, J. Ning, B. Luo, B. Wang, Y. Zhang, Z. Tang, J. Yang, A. Thomas, L. Zhi, Structural evolution of 2D microporous covalent triazine-based framework toward the study of high-performance supercapacitors, *J. Am. Chem. Soc.* 137 (2015) 219–225, <https://doi.org/10.1021/ja508693y>.
- [37] S. Abednatanzi, P.G. Derakhshandeh, K. Leus, H. Vrieland, F. Callens, J. Schmidt, A. Savateev, P. Van Der Voort, Metal-free activation of molecular oxygen by covalent triazine frameworks for selective aerobic oxidation, *Sci. Adv.* 6 (2020), eaaz2310, <https://doi.org/10.1126/sciadv.aaz2310>.
- [38] Y. Li, S. Zheng, X. Liu, P. Li, L. Sun, R. Yang, S. Wang, Z.-S. Wu, X. Bao, W.-Q. Deng, Conductive microporous covalent triazine-based framework for high-performance electrochemical capacitive energy storage, *Angew. Chem., Int. Ed.* 57 (2018) 7992–7996, <https://doi.org/10.1002/anie.201711169>.
- [39] S. Hug, L. Stegbauer, H. Oh, M. Hirscher, B.V. Lotsch, Nitrogen-rich covalent triazine frameworks as high-performance platforms for selective carbon capture and storage, *Chem. Mater.* 27 (2015) 8001–8010, <https://doi.org/10.1021/acs.chemmater.5b03330>.
- [40] Y.J. Lee, S.N. Talapaneni, A. Coskun, Chemically activated covalent triazine frameworks with enhanced textural properties for high-capacity gas storage, *ACS Appl. Mater. Interfaces* 9 (2017) 30679–30685, <https://doi.org/10.1021/acsami.7b08930>.
- [41] X. Lan, Y. Li, C. Du, T. She, Q. Li, G. Bai, Porous carbon nitride frameworks derived from covalent triazine framework anchored Ag nanoparticles for catalytic CO<sub>2</sub> conversion, *Chem. Eur. J.* 25 (2019) 8560–8569, <https://doi.org/10.1002/chem.201900563>.

- [42] A. Bhunia, V. Vasylyeva, C. Janiak, From a supramolecular tetranitrile to a porous covalent triazine-based framework with high gas uptake capacities, *Chem. Commun.* 49 (2013) 3961–3963, <https://doi.org/10.1039/C3CC41382A>.
- [43] S. Dey, A. Bhunia, H. Breitzke, P.B. Groszewicz, G. Buntkowsky, C. Janiak, Two linkers are better than one: enhancing CO<sub>2</sub> capture and separation with porous covalent triazine-based frameworks from mixed nitrile linkers, *J. Mater. Chem. A* 5 (2017) 3609–3620, <https://doi.org/10.1039/C6TA07076K>.
- [44] X.-M. Hu, Q. Chen, Y.-C. Zhao, B.W. Laursen, B.-H. Han, Straightforward synthesis of a triazine-based porous carbon with high gas-uptake capacities, *J. Mater. Chem. A* 2 (2014) 14201–14208, <https://doi.org/10.1039/C4TA02073A>.
- [45] J. Jia, Z. Chen, Y. Belmabkhout, K. Adil, P.M. Bhatt, V.A. Solovyeva, O. Shekhan, M. Eddaoudi, Carbonization of covalent triazine-based frameworks via ionic liquid induction, *J. Mater. Chem. A* 6 (2018) 15564–15568, <https://doi.org/10.1039/C8TA05583A>.
- [46] H.R. Abuzeid, A.F.M. EL-Mahdy, M.M.M. Ahmeda, S.-W. Kuo, Triazine-functionalized covalent benzoxazine framework for direct synthesis of N-doped microporous carbon, *Polym. Chem.* 10 (2019) 6010–6020, <https://doi.org/10.1039/C9PY01231A>.
- [47] M. Kim, P. Puthiaraj, Y. Qian, Y. Kim, S. Jang, S. Hwang, E. Na, W.S. Ahn, S. E. Shim, High performance carbon supercapacitor electrodes derived from a triazine-based covalent organic polymer with regular porosity, *Electrochim. Acta* 284 (2018) 98–107, <https://doi.org/10.1016/j.electacta.2018.07.096>.
- [48] P. Puthiaraj, W.S. Ahn, Facile synthesis of microporous carbonaceous materials derived from a covalent triazine polymer for CO<sub>2</sub> capture, *J. Energy Chem.* 26 (2017) 965–971, <https://doi.org/10.1016/j.jechem.2017.07.012>.
- [49] Z. Zhang, S. Yao, X. Hu, F. Okeji, K. He, P. Liu, Z. Tian, V.P. Dravid, J. Fu, X. Zhu, S. Dai, Sacrificial synthesis of supported Ru single atoms and clusters on N-doped carbon derived from covalent triazine frameworks: a charge modulation approach, *Adv. Sci.* 8 (2021), 2001493, <https://doi.org/10.1002/advs.202001493>.
- [50] L. Hao, S. Zhang, R. Liu, J. Ning, G. Zhang, L. Zhi, Bottom-up construction of triazine-based frameworks as metal-free electrocatalysts for oxygen reduction reaction, *Adv. Mater.* 27 (2015) 3190–3195, <https://doi.org/10.1002/adma.201500863>.
- [51] Y. Jiao, Z. Ye, F. Wu, A. Xie, W. Zhao, L. Wu, X. Zhu, W. Dong, Conjugate microporous polymer-derived conductive porous carbon nanoparticles with narrow pore-size distribution for electromagnetic interference shielding, *ACS Appl. Nano Mater.* 3 (2020) 4553–4561, <https://doi.org/10.1021/acsnm.0c00624>.
- [52] L. Jiao, Y. Hu, H. Ju, C. Wang, M.-R. Gao, Q. Yang, J. Zhu, S.-H. Yu, H.-L. Jiang, From covalent triazine-based frameworks to N-doped porous carbon/reduced graphene oxide nanosheets: efficient electrocatalysts for oxygen reduction, *J. Mater. Chem. A* 5 (2017) 23170–23178, <https://doi.org/10.1039/c7ta07387a>.
- [53] D. Baumann, C. Lee, C. Wan, H. Sun, X. Duan, Hierarchical porous carbon derived from covalent triazine frameworks for high mass loading supercapacitors, *ACS Mater. Lett.* 1 (2019) 320–326, <https://doi.org/10.1021/acsmaterialslett.9b00157>.
- [54] K. Yuan, T. Hu, Y. Xu, R. Graf, L. Shi, M. Forster, T. Pichler, T. Riedl, Y. Chen, U. Scherf, Nitrogen-doped porous carbon/graphene nanosheets derived from two-dimensional conjugated microporous polymer sandwiches with promising capacitive performance, *Mater. Chem. Front.* 1 (2017) 278–285, <https://doi.org/10.1039/c6qm00012f>.
- [55] L. Yang, J. Shui, L. Du, Y. Shao, J. Liu, L. Dai, Z. Hu, Carbon-based metal-free ORR electrocatalysts for fuel cells: past, present, and future, *Adv. Mater.* 31 (2019) 1804799, <https://doi.org/10.1002/adma.201804799>.
- [56] X. Zhu, C. Hu, R. Amal, L. Dai, X. Lu, Heteroatom-doped carbon catalysts for zinc–air batteries: progress, mechanism, and opportunities, *Energy Environ. Sci.* 13 (2020) 4536–4563, <https://doi.org/10.1039/d0ee02800b>.
- [57] X. Zhao, H. Zhang, Y. Yan, J. Cao, X. Li, S. Zhou, Z. Peng, J. Zeng, Engineering the electrical conductivity of lamellar silver-doped cobalt(II) selenide nanobelts for enhanced oxygen evolution, *Angew. Chem., Int. Ed.* 56 (2017) 328–332, <https://doi.org/10.1002/anie.201609080>.
- [58] S.K. Singh, K. Takeyasu, J. Nakamura, Active sites and mechanism of oxygen reduction reaction electrocatalysis on nitrogen-doped carbon materials, *Adv. Mater.* 31 (2019), 1804297, <https://doi.org/10.1002/adma.201804297>.
- [59] L. Lai, J.R. Potts, D. Zhan, L. Wang, C.K. Poh, C. Tang, H. Gong, Z. Shen, J. Linc, R. S. Ruoff, Exploration of the active center structure of nitrogen-doped graphene-based catalysts for oxygen reduction reaction, *Energy Environ. Sci.* 5 (2012) 7936–7942, <https://doi.org/10.1039/C2EE21802J>.
- [60] X. Mou, J. Ma, S. Zheng, X. Chen, F. Krumeich, R. Hauert, R. Lin, Z.-S. Wu, Y. Ding, A general synthetic strategy toward highly doped pyridinic nitrogen-rich carbons, *Adv. Funct. Mater.* 31 (2021), 2006076, <https://doi.org/10.1002/adfm.202006076>.
- [61] X. Zhang, J. Luo, H.-F. Lin, P. Tang, J.R. Morante, J. Arbiol, K. Wan, B.-W. Mao, L.-M. Liu, J. Fransser, Tailor-made metal-nitrogen-carbon bifunctional electrocatalysts for rechargeable Zn–air batteries via controllable MOF units, *Energy Storage Mater.* 17 (2019) 46–61, <https://doi.org/10.1016/j.ensm.2018.11.034>.
- [62] Y.-N. Wang, Z.-J. Yang, D.-H. Yang, L. Zhao, X.-R. Shi, G. Yang, B.-H. Han, FeCoP<sub>2</sub> nanoparticles embedded in N and P co-doped hierarchically porous carbon for efficient electrocatalytic water splitting, *ACS Appl. Mater. Interfaces* 13 (2021) 8832–8843, <https://doi.org/10.1021/acsaami.0c22336>.
- [63] H. Liu, D.-H. Yang, X.-Y. Wang, J. Zhang, B.-H. Han, N-doped graphitic carbon shell-encapsulated FeCo alloy derived from metal–polyphenol network and melamine sponge for oxygen reduction, oxygen evolution, and hydrogen evolution reactions in alkaline media, *J. Colloid Interface Sci.* 581 (2021) 362–373, <https://doi.org/10.1016/j.jcis.2020.07.055>.
- [64] Y.-N. Sun, M.-L. Zhang, L. Zhao, Z.-Y. Sui, Z.-Y. Sun, B.-H. Han, A N, P dual-doped carbon with high porosity as an advanced metal-free oxygen reduction catalyst, *Adv. Mater. Interfaces* 6 (2019), 1900592, <https://doi.org/10.1002/admi.201900592>.
- [65] H. Jiang, J. Gu, X. Zheng, M. Liu, X. Qiu, L. Wang, W. Li, Z. Chen, X. Ji, J. Li, Defect-rich and ultrathin N-doped carbon nanosheets as advanced trifunctional metal-free electrocatalysts for the ORR, OER, and HER, *Energy Environ. Sci.* 12 (2019) 322–333, <https://doi.org/10.1039/c8ee03276a>.
- [66] Y. Arafat, M.R. Azhar, Y. Zhong, M.O. Tadé, Z. Shao, Metal-free carbon-based air electrodes for Zn–air batteries: recent advances and perspective, *Mater. Res. Bull.* 140 (2021), 111315, <https://doi.org/10.1016/j.materresbull.2021.111315>.
- [67] Q. Yang, Q. Li, Z. Liu, D. Wang, Y. Guo, X. Li, Y. Tang, H. Li, B. Dong, C. Zhi, Dendrites in Zn-based batteries, *Adv. Mater.* 32 (2020), 2001854, <https://doi.org/10.1002/adma.202001854>.
- [68] W. Sun, F. Wang, B. Zhang, M. Zhang, V. Küpers, X. Ji, C. Theile, P. Bieker, K. Xu, C. Wang, M. Winter, A rechargeable zinc–air battery based on zinc peroxide chemistry, *Science* 371 (2021) 46–51, <https://doi.org/10.1126/science.abb9554>.
- [69] P. Sun, J. Chen, Y. Huang, J.-H. Tian, S. Li, G. Wang, Q. Zhang, Z. Tian, L. Zhang, High-strength agarose gel electrolyte enables long-endurance wearable Al–air batteries with greatly suppressed self-corrosion, *Energy Storage Mater.* 34 (2021) 427–435, <https://doi.org/10.1016/j.ensm.2020.10.009>.